JOM, Vol. 71, No. 10, 2019
https://doi.org/10.1007/s11837-019-03715-1




# Selective Laser Melting of $Al_{0.3}CoCrFeNi$ High-Entropy Alloy: Printability, Microstructure, and Mechanical Properties

FLORIAN PEYROUZET,[1,2] DORIAN HACHET,[3] ROMAIN SOULAS,[1] CHRISTELLE NAVONE,[1] STÉPHANE GODET,[3] and STÉPHANE GORSSE [2,4]

1.—LITEN, CEA, 38054 Grenoble, France. 2.—Univ. Bordeaux, CNRS, Bordeaux INP, ICMCB, UMR 5026, 33600 Pessac, France. 3.—Service 4MAT, Université libre de Bruxelles, 1050 Brussels, Belgium. 4.—e-mail: stephane.gorsse@icmcb.cnrs.fr

$Al_{0.3}CoCrFeNi$ high-entropy alloy (HEA) was additively manufactured by powder-bed selective laser melting (SLM) with emphasis on its microstructure and tensile properties. $Al_{0.3}CoCrFeNi$ showed excellent printability, enabling fabrication of fully dense products. The microstructure of the SLM as-built HEA consisted of a single-phase disordered face-centered cubic solid solution with fine columnar grains elongated along the build direction. The characteristic features of the as-built microstructure were a <110> fiber texture aligned toward the build direction and a large dislocation density. As a consequence, printed $Al_{0.3}CoCrFeNi$ HEA exhibited superior tensile strength in comparison with as-cast or wrought counterparts.

## INTRODUCTION

The high-entropy alloy (HEA)[1,2] and complex concentrated alloy (CCA)[3] concepts offer the designer new options for advanced materials with better structural properties.[4–6] While the HEA approach focuses on a single disordered solid-solution phase, CCAs can exhibit multiphase microstructures and encompass HEAs. We do not distinguish between HEA and CCA herein, preferring to use the term HEA. Rather than using one principal element as an alloy base, HEAs/CCAs consist of a concentrated blend of at least three principal elements acting as one alloy "hybrid base." This paradigm change has several important consequences[7]: (i) the 67 stable metallic elements give a total of over 110 million new alloy bases with three, four, five, or six principal elements, and (ii) the exploration of the composition space is shifted from the boundaries of multicomponent phase diagrams to the vast and uncharted central regions.

So far, among the new alloy families that have emerged, the 3*d* transition metal (TM) family, which derivates from the Cantor alloy, i.e., CoCrFeMnNi face-centered-cubic (FCC) solid-solution phase, have attracted great attention because of their attractive mechanical performance. Indeed, 3*d* TM HEAs/CCAs can be regarded as an extension of austenitic stainless steels, austenitic nickel alloys, and nickel-based superalloys. Whereas a great deal of work is currently underway on additive manufacturing of these three conventional alloy classes, three-dimensional (3D) printing of 3*d* TM HEAs/CCAs has received much less attention.[8–18] In this paper, we explore the microstructure and tensile properties of $Al_{0.3}CoCrFeNi$ HEA processed by powder-bed selective laser melting (SLM). Our alloy selection is motivated by the exceptional tunability principle of this FCC-based HEA, which has been demonstrated for wrought products; i.e., multiphase FCC-$L1_2$, FCC-B2 or FCC-B2-$\sigma$ microstructures can be generated by tuning the cold rolling percentage and annealing temperature.[19–21] The vast range of microstructures and mechanical properties that can be achieved with $Al_{0.3}CoCrFeNi$ HEA makes it a prime candidate for additive manufacturing. In the SLM process, the part is built layer by layer using a laser beam that scans over a metal powder bath. The metal melts at every point under the laser beam track and then rapidly solidifies. This rapid solidification of a small melt pool under conditions of anisotropic heat removal can have important consequences for the microstructure of the printed components. The emphasis of the current work is on the microstructure and texture features of additively manufactured $Al_{0.3}CoCrFeNi$ alloy. We

(Published online August 5, 2019)

evaluate the printability and highlight the mechanical properties of as-built specimens in comparison with as-cast and wrought conditions.

## EXPERIMENTAL PROCEDURES

$Al_{0.3}$CoCrFeNi HEA samples were additively manufactured using gas-atomized prealloyed powder with composition 6Al-24.4Co-23.9Cr-21.6Fe-24.1Ni (at.%) provided by DUCAL. The spherical morphology (powder circularity 0.92) of the powders containing few satellites is shown in Fig. S1 in the Electronic Supplementary Material. The median particle diameter $D_{50}$ was 29 $\mu$m with a size distribution ranging from $D_{10}$ = 20 $\mu$m to $D_{90}$ = 42 $\mu$m. The x-ray diffraction (XRD) pattern (Fig. S2a in Electronic Supplementary Material) reveals a single phase with face-centered cubic (FCC) lattice structure. The single-phase FCC microstructure is further confirmed by the electron backscattered diffraction (EBSD) phase map (Fig. S2b in Electronic Supplementary Materials) obtained by field-emission gun-scanning electron microscopy (FEG-SEM; Hitachi, at 20 kV). The measured total reflectivity of the atomized $Al_{0.3}$CoCrFeNi HEA powder at the laser wavelength was 25%.

Specimens with dimensions of 10 mm × 10 mm × 10 mm (Fig. S3a in Electronic Supplementary Material) were produced by SLM in an argon environment ($O_2$ content < 300 ppm) using a PROX DMP 200 machine (3D Systems instrument) equipped with a laser with wavelength of $\lambda$ = 1065 nm and spot size of 70 $\mu$m. Stainless-steel fabrication substrates were used without preheating. The powder was heated at 110°C for 2 h under vacuum prior to printing. The machine was operated with hatch spacing $h$ of 45 $\mu$m, layer thickness $t$ between 25 $\mu$m to 30 $\mu$m, scan speed $v$ between 1100 mm/s and 1300 mm/s, and laser power $P$ between 150 W and 170 W, resulting in a volumetric energy density, $E = P/vht$, ranging from 85 J/mm$^3$ to 137 J/mm$^3$. A scan strategy with a unidirectional scanning vector and a 67° rotation between consecutive layers was applied. The density of the fabricated specimens was determined by Archimedes' method, and the porosity was characterized by 3D x-ray microtomography on a Nanotom GE. The aim of this screening was to obtain fully dense alloys.

The microstructure was observed using a MERLIN (ZEISS) scanning electron microscope (SEM) on mirror surface-polished samples achieved using 0.03-$\mu$m colloidal silica. Transmission electron microscopy (TEM) investigations were conducted with a Tecnai Osiris instrument and on ASTAR.

Foils were extracted from specimens along the build direction and punched with a hydraulic press. The thickness of the foils was reduced to about 100 $\mu$m for both sides using SiC paper (P4000). Electropolishing with perchloric acid and ethanol under 20 V was used to complete the polishing, until obtaining electron-transparent regions.

Room-temperature tensile tests were performed at strain rate of $5 \times 10^{-4}$ s$^{-1}$, on round-cross-section specimens with gauge diameter of 4 mm and gauge length of 22 mm, machined from 10 mm × 10 × mm × 45 mm samples with longitudinal axis perpendicular to the build direction (Fig. S3b in Electronic Supplementary Material) and fabricated using optimal printing conditions ($P$ = 160 W, $v$ = 1100 mm/s, $t$ = 25 $\mu$m).

## RESULTS AND DISCUSSION

### Microstructure of As-Built SLM $Al_{0.3}$CoCrFeNi HEA

The density of the SLM-processed HEA samples measured using Archimedes' principle was 7.76 g/cm$^3$, which represents 99.9% of the theoretical density. This very good consolidation was confirmed by 3D x-ray microtomography, which showed no detectable pores. SEM images also showed dense microstructure without visible porosity.

In the XRD profiles (Fig. 1a and b) of the as-built SLM HEA, only FCC phase with lattice parameter $a$ = 3.59 Å was detected. The EBSD phase map (Fig. 1c) did not reveal the presence of any second phase. TEM examination showed that the microstructure was free of precipitates. Based on the calculated phase diagram (Fig. S4 in Electronic Supplementary Material), it can be stated that the microstructure consisted of one FCC supersaturated solid solution. The presence of a single supersaturated FCC solid solution in the as-printed state while the alloy is located in the multiphase phase field below 1120°C is thought to result from the fast cooling rate associated with the solidification of a small melt pool.

The XRD peak intensity distribution taken from the plane perpendicular (Fig. 1a) to the build direction and parallel (Fig. 1b) are different, which suggests that the as-printed samples possess crystallographic texture. This is confirmed by the EBSD inverse pole figure (IPF) and pole figure (PF) maps taken from a plane perpendicular to the build direction (Fig. 2a and b) and parallel (Fig. 2c and d). The {110} pole figure (Fig. 2b) taken on the surface perpendicular to the build direction shows a strong peak of the <110> intensity along the $z$-direction (which is the build direction) in addition to an inner ring-like distribution. This evidences that a <110> fiber texture oriented towards the build direction was developed in the printed HEA. At first thought, this crystallographic texture is unexpected because the <001> direction is the prominent observation in additively manufactured FCC alloys. For example, laser-melted single-phase FCC CoCrFeMnNi[15] and laser-deposited single-phase FCC

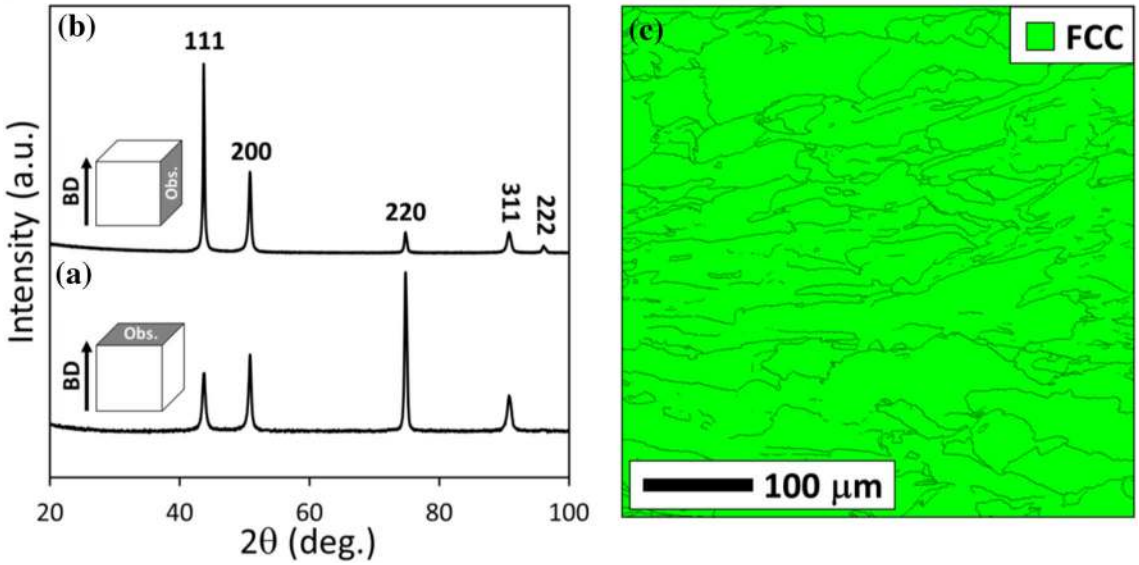


Fig. 1. XRD patterns of as-built SLM-processed $Al_{0.3}CoCrFeNi$ samples taken from the plane perpendicular to the build direction (a) and parallel (b). (c) EBSD phase maps (using green color for FCC phase) for as-built $Al_{0.3}CoCrFeNi$ alloy processed by SLM.

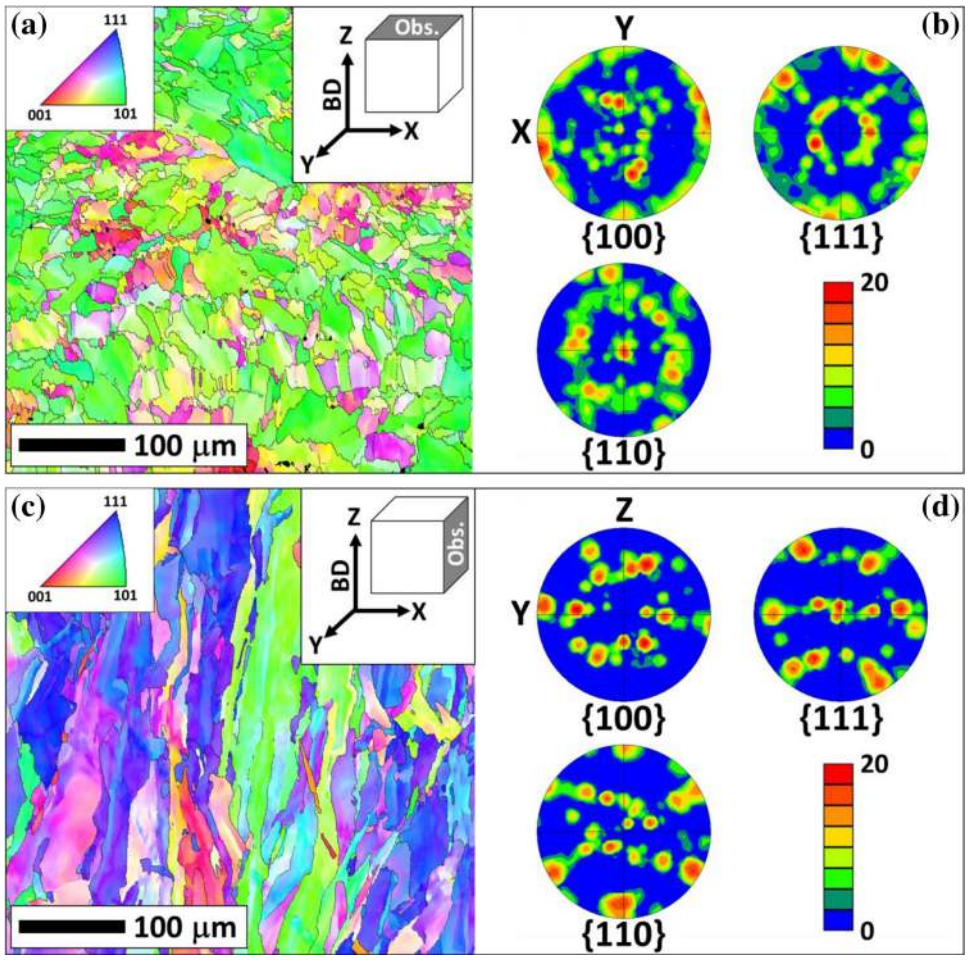


Fig. 2. EBSD IPF-Z (a, c) and PF (b, d) maps taken from as-built FCC $Al_{0.3}CoCrFeNi$ prepared using SLM, highlighting the $<110>$ fiber texture towards the sample build direction: (a, b) the plane of the map is perpendicular to the build direction and (c, d) parallel.

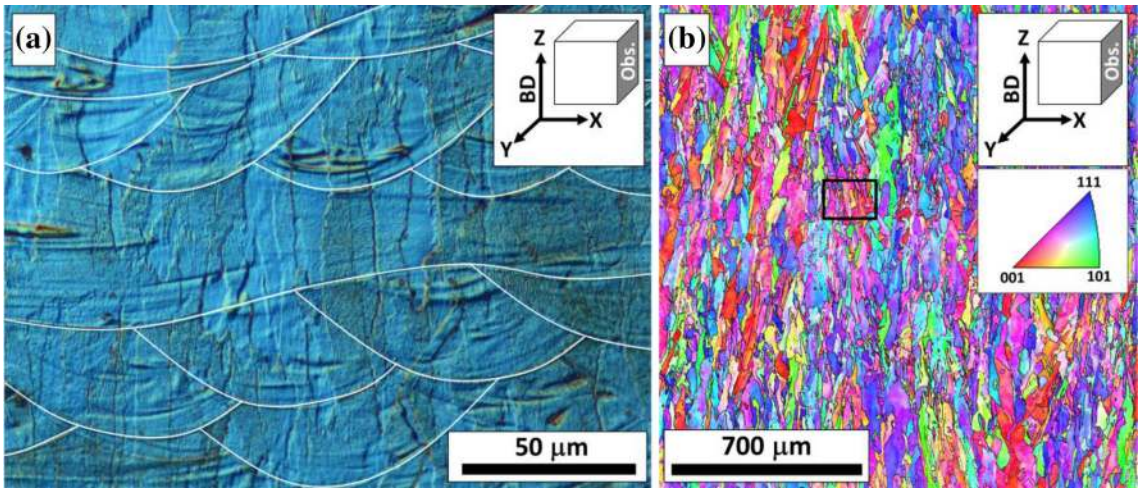


Fig. 3. (a) Optical image showing the columnar cells and the traces of the melt pools observed in a plane parallel to the build direction. (b) Low-magnification EBSD IPF-Z map showing random crystal orientation in a plane parallel to the build direction. The black frame indicates the size of the optical micrograph shown in (a).

$Al_{0.3}$CoCrFeNi HEAs[11] both showed a <001> fiber texture parallel to the build direction, as do many conventional FCC alloys.[22,23] In the same vein, the columnar zone in ingots of FCC alloys exhibits <001> orientation. The origin of the <001> solidification texture is that the preferred growth direction in FCC crystals is <001>, so grains with <001> orientation aligned to the maximum heat flux during solidification are favored and overgrow misaligned ones.

To explain the formation mechanism of the <110> texture observed in the present printed HEA, further investigations were carried out. Figure 3 shows an optical micrograph of the longitudinal cross-section of the printed HEA (with the build direction vertical). This image displays the melt pool traces from several adjacent scan tracks distributed within five neighboring layers. The solidification microstructure consists of columnar cells more or less aligned along the build direction, within elongated grains developed across a few successive layers, which indicates epitaxial growth. These elongated grains (with average width of 13 $\mu$m and length ranging between 70 $\mu$m and 120 $\mu$m) result in the development of the <110> texture along the build direction. Previous studies offer interesting insights to explain this dominant crystallographic orientation. Piglione et al.[14] and Andreau et al.[24] both observed concurrent <110> and <001> fiber texture along the build direction in CoCrFeMnNi HEA and 316L printed by SLM using a bidirectional scanning pattern without rotation that differs from the one applied in the present work (unidirectional scanning with 67° rotation). The rational is that the preferred growth direction (<001> for FCC crystals) is aligned with the local direction of maximum heat extraction. As a result, the grains grow towards the direction perpendicular to the melt pool profile (i.e., the elliptic solid–liquid interface) and point towards the center of the melt pool. At the bottom of the melt pool, grains grow with <001> orientation along the build direction, while on the sides of the melt pool, grains with <001> orientation inclined at 45° with respect to the build direction lead to development of <110> fiber texture aligned with the build direction.[14,25]

Several authors have reported that the effects of the melt pool shape and thermal gradient on the crystallographic texture can be influenced by the processing parameters. In this regard, the preferred crystal orientation along the build direction can be varied from <001> to <110> by increasing the laser power in 316L stainless steel printed by SLM,[25] or by varying the scanning strategy in SLM Ni-Mo alloys[26]; i.e., <001> is preferred in bidirectional scanning with rotation in each layer, while <110> is favored in bidirectional scanning along one axis (without rotation between each layer). During bidirectional laser scanning along one axis (no rotation), the development of <110> texture is generally associated with a zigzag solidification pattern because dendrites with <100> direction in the next layer grow perpendicular to the dendrites in the previous layer.[27] In this work, unidirectional scanning with 67° rotation was applied. Note that, under such conditions, the profiles and centers of the melt pools change from one layer to another due to the 67° rotation in each layer, which causes random orientations of the grains in the plane perpendicular to the build direction (Fig. 3b) and prevents development of zigzag solidification pattern.

It is apparent from the comparison between the microstructures obtained in the present work and those from additively manufactured FCC alloys (both HEAs and conventional alloys) that different

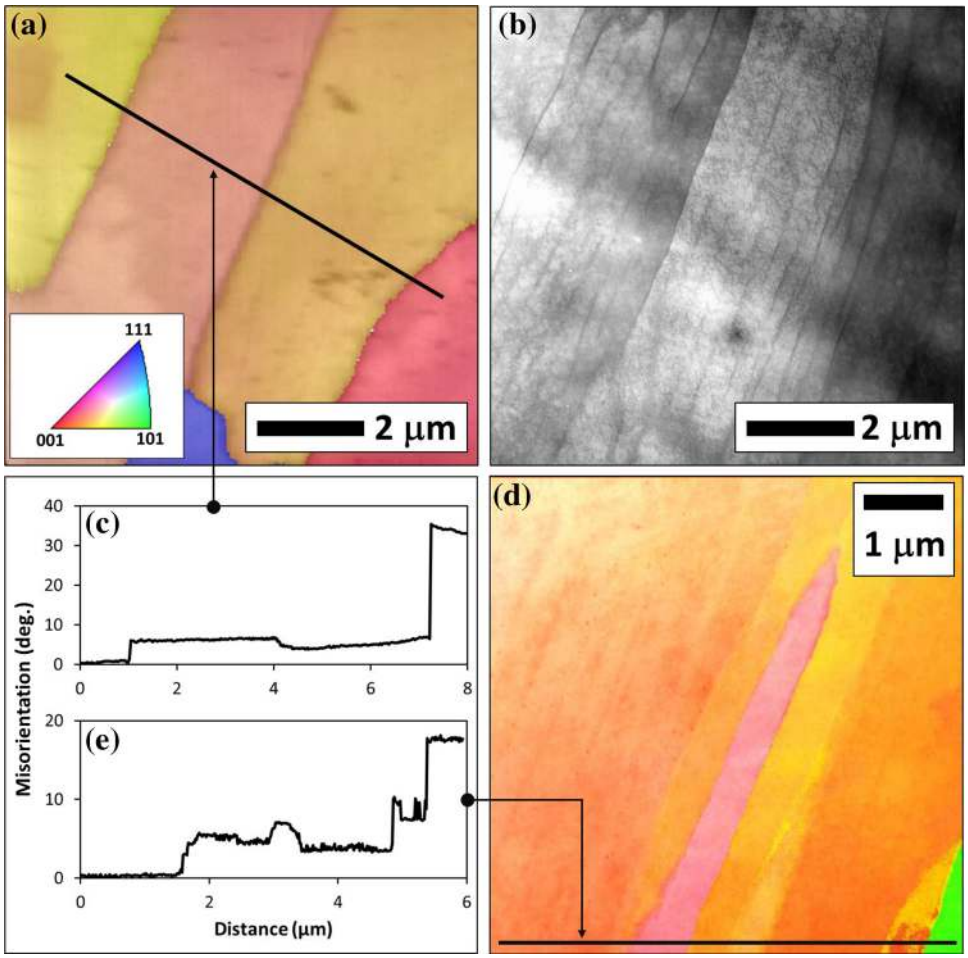


Fig. 4. Series of images showing the hierarchical microstructure of the as-built SLM $Al_{0.3}CoCrFeNi$ HEA observed in a plane parallel to the build direction. (a) EBSD IPF orientation map and (b) TEM bright-field images of several colonies of cells. (c) Misorientation profile across several cells from the line in (a). (d) EBSD-TEM crystal orientation map and (e) misorientation profile across several cells performed on ASTAR.

crystallographic textures can be generated in fully dense additively manufactured HEA products through control of the process parameters, which opens up new opportunities to tailor the microstructure and tune the resulting properties of the additively manufactured parts. The tuning parameters include the laser scan strategy used in melting each successive layer,[26,28] the laser power,[25] the hatch spacing,[29] and the shielding gas flow direction.[24] From the analysis above, it can be deduced that the most straightforward strategy to develop a stronger texture or change the preferred orientation towards the build direction would be to apply a bidirectional scanning pattern with 0° or 90° rotation, and/or increase the laser power.

Figures 3 and 4 depict the hierarchical microstructure of the as-built SLM HEA characterized by a subgrain cellular structure inside the columnar grains which have grown towards the build direction. The width of the elongated cells is approximatively 400 nm, being arranged in colonies in which the cells are aligned towards the same direction and have small crystallographic misorientation of about 2°–7° with respect to their neighbors. Colonies of cells can have high-angle grain boundaries with crystallographic misorientation above 15° or low-angle boundaries with crystallographic misorientation below 15°. This type of subgrain cellular structure is observed in many additively manufactured alloys and generally results from solute segregation during cellular grain growth.[29–32] It is often found that a high density of dislocation is stored in this type of cellular structure, which influences the mechanical properties.[29,31, 32]

## Mechanical Properties

Figure 5 shows the room-temperature engineering and true stress–strain curves of the as-built $Al_{0.3}CoCrFeNi$ HEA tested in tension normal to the build direction. The additively manufactured alloy has much higher strength (engineering yield strength, $\sigma_y$ = 730 MPa and engineering ultimate tensile strength, $\sigma_{UTS}$ = 896 MPa) compared with the same alloy in as-cast ($\sigma_y$ = 275 MPa)[33] or wrought and recrystallized[21] (cold-rolled and annealed, $\sigma_y$ = 159 MPa) state, while retaining

significant ductility (29%, engineering value). The fracture surface (Fig. 6) exhibits dimples that are about the size of cellular regions, resulting from ductile failure. In the three conditions (i.e., as-built SLM, as cast, and recrystallized), the microstructures are 100% austenitic (single-phase FCC) and fully dense. In the printed alloy, the columnar grains are oriented perpendicular to the tensile test direction. Their average width is 13 $\mu$m, which is significantly finer than the grain size observed in cast ($\sim$ 50 $\mu$m[33]) or recrystallized (100 $\mu$m)[21] equivalents. Even though the grain size influences the mechanical response, it is very unlikely that Hall–Petch strengthening alone can explain the tripling of the yield strength for as-built SLM alloy compared with coarser-grained as-cast or recrystallized counterparts.

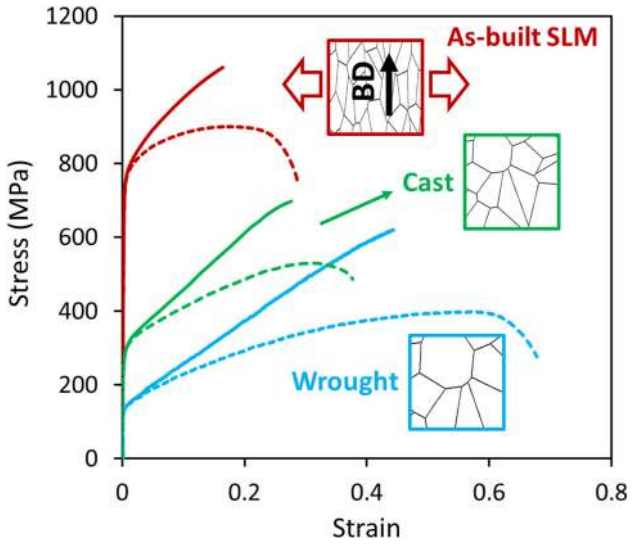


Fig. 5. Room-temperature tensile properties of $Al_{0.3}CoCrFeNi$ in as-built SLM (red curves), as-cast (green curves[33]), and wrought and recrystallized (blue curves[21]) state: (a) engineering stress versus engineering plastic strain (dashed lines) and (b) true stress versus true strain curves (solid lines).

Yield stress is a combination of several strengthening contributions: intrinsic lattice resistance to dislocation motion ($\sigma_i$), solid solution ($\Delta\sigma_{ss}$), grain boundary (Hall–Petch, $\Delta\sigma_{gb} = k_y/\sqrt{D}$, where $k_y$ is a material constant and $D$ is the grain size), dislocations ($\Delta\sigma_d$), and precipitates ($\Delta\sigma_p$). Since no second phase was observed in the present as-built HEA, the yield strength of the single-phase FCC $Al_{0.3}$CoCrFeNi HEA can be expressed as

$$\sigma_y = \sigma_i + \Delta\sigma_{ss} + \Delta\sigma_{gb} + \Delta\sigma_d = \sigma_0 + \Delta\sigma_{gb} + \Delta\sigma_d \quad (1)$$

where $\sigma_0$ includes the intrinsic lattice resistance to dislocation motion and the contribution due to solid-solution hardening. Ma et al.[33] reported a value of $\sigma_0$ = 172 MPa and a Hall–Petch coefficient $k_y$ = 0.73 MPa/m$^{1/2}$ for the as-cast single-phase FCC $Al_{0.3}$CoCrFeNi HEA. Thus, one would expect that the decrease of the grain size from 50 $\mu$m to 13 $\mu$m for the as-built alloy as compared with the as-cast state would cause an increase of the yield strength from 275 MPa to 383 MPa (Table S1 in Electronic Supplementary Material), which represents only half of the measured yield strength of the as-built HEA. This suggests the key role of forest dislocations in the printed alloy.

The TEM observations (Fig. 7) provide interesting insights. The boundaries of subgrains observed in Fig. 4 result from a nonuniform distribution of dislocations which cluster into cell walls. This fine dislocation cell structure is characterized by substantial internal misorientation within the grains, which suggests that they are heavily deformed, as shown by the EBSD grain orientation spread (GOS) map and misorientation profile (Fig. 8a). Using TEM, the dislocation density was estimated from the total projected length of the dislocation lines, $l'$,

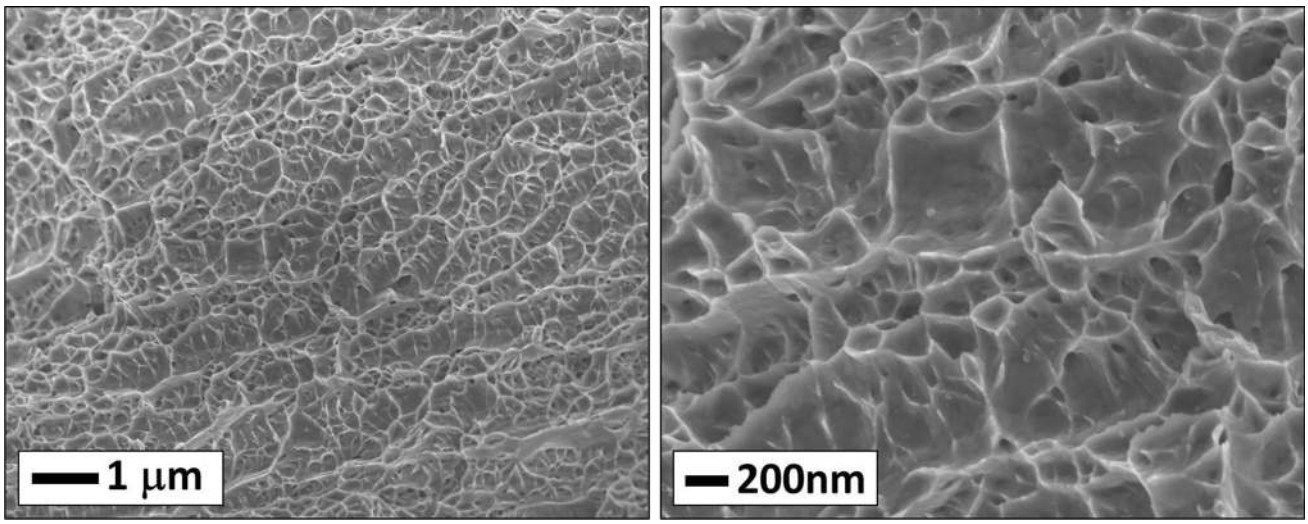


Fig. 6. Low- and high-magnification SEM images of the fracture surface of as-built SLM $Al_{0.3}$CoCrFeNi alloy tested in tension normal to the build direction, at room temperature. The plane of the image is parallel to the build direction.

in a given area $A$ of a given thickness $t$ using the relationship

$$\rho = \frac{4}{\pi}\frac{l'}{At}. \quad (2)$$

The overall dislocation density is found to lie in the range from $3 \times 10^{14}$ m/m$^3$ to $7 \times 10^{14}$ m/m$^3$. Estimates obtained from the XRD profiles using the equations derived by Williamson and Hall[34] and Williamson and Smallman[35] give similar values of about $4 \times 10^{14}$ m$^{-2}$. Such high density of dislocations in SLM metals is very likely when compared with the value of about $1 \times 10^{15}$ m$^{-2}$ observed in as-built 316L steel obtained by SLM.[8,31]

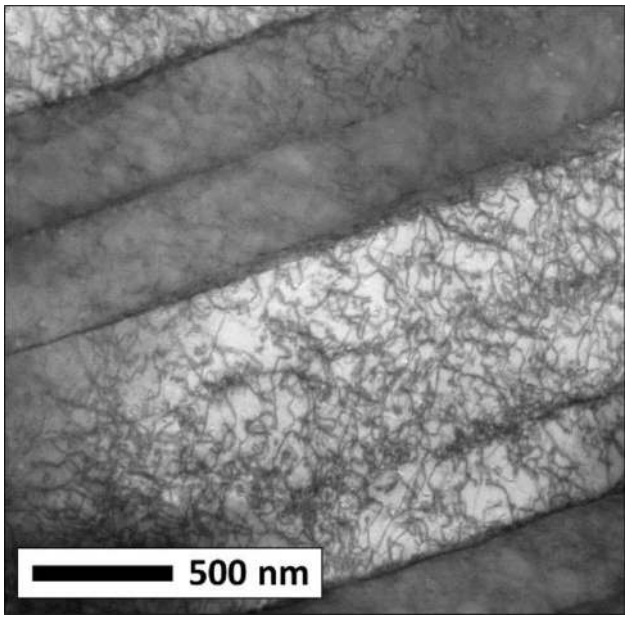


Fig. 7. TEM bright-field images of microstructure of as-built SLM $Al_{0.3}CoCrFeNi$. The plane of the image is parallel to the build direction.

The contribution of the dislocation density to the flow stress may be estimated using Taylor's equation $\sigma_d = M\alpha Gb\sqrt{\rho}$, where $M$ is the Taylor factor that accounts for the averaging of the grain orientations over all grains in the sample. Its value ranges from 3.063 for random orientations to 3.674 for perfect <110> texture.[36] The <110> fiber texture observed parallel to the build direction indicates a strong hardening response to uniaxial traction, as shown by the large number of grains presenting high Taylor factors (Fig. 8b). Since the Taylor factor of a polycrystalline textured material is given by the mean value of the Taylor factors of all orientations present in the material, we fixed $M$ = 3.3 to reflect the nonideality of the observed <110> fiber texture of the as-built SLM samples. $\alpha$ is a correlation factor specific to the material, taken equal to 0.2.[37] The shear modulus $G$ was estimated between to lie between 83 GPa and 88 GPa using the rule of mixtures for single-phase solid solution (i.e., $G = x_iG_i$ where $x_i$ is the atomic fraction and $G_i$ is the shear modulus of alloy element $i$) and from the measured Young's modulus $E$ = 230 GPa using the expression $G = E/2(1 + \upsilon)$, where $\upsilon$ is the Poisson coefficient with value fixed to 0.3. The magnitude of the Burgers vector for {111} <110> planar slip is $b = a/\sqrt{2} = 0.254$ nm. Using these values, Taylor's equation gives an estimate of between 240 MPa and 390 MPa for the strengthening contribution arising from the interaction between dislocations. Hence, the total yield strength is estimated to range between 624 MPa and

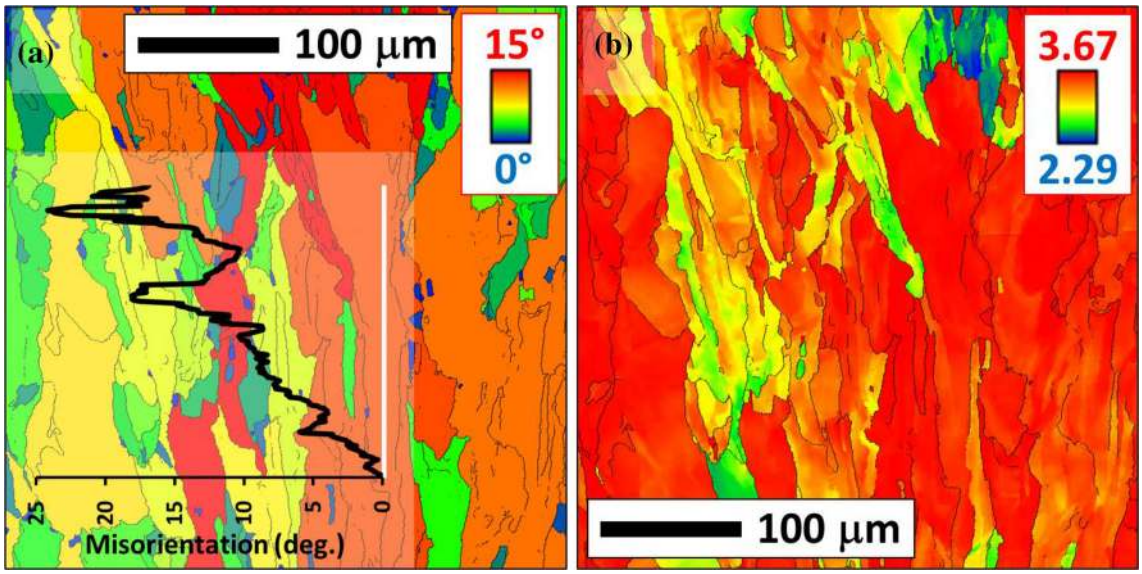


Fig. 8. EBSD maps of as-built SLM $Al_{0.3}CoCrFeNi$ taken in plane parallel to the build direction: (a) grain orientation spread (GOS) and (b) Taylor factors. The misorientation profile drawn along a grain is shown with a white line on the GOS map. Cell walls with misorientations of 2°–6° coupled with intracell misorientations at the same order of magnitude lead to intragrain misorientations reaching 25°.

775 MPa, which compares well with the measured value of 730 MPa. Although the refined grain size contributes significantly to the yield strength of as-built SLM HEA, the present calculations reveal that the most important contribution arises from forest dislocations, combined with the effect of anisotropy due to the crystallographic texture. The explanation offered in literature for the high dislocation density is that it is due to thermal contraction strain during rapid solidification.[8]

## CONCLUSION

The $Al_{0.3}CoCrFeNi$ HEA was additively manufactured by SLM using prealloyed gas-atomized powder. The characteristics of the powder ensure a good compacity of the powder bed and absorption of the laser beam, which results in excellent processability of the HEA. The rapid solidification and anisotropic heat removal give rise to a fully dense, FCC single-phase microstructure with fine and elongated grains. The most remarkable microstructural features of the as-built samples are (i) the <110> fiber texture aligned with the build direction and (ii) the high density of dislocations. Rationalization of the grain orientations suggests a way to tailor the crystallographic texture by tuning the printing parameters. The room-temperature yield strength and ultimate tensile strength are greatly improved for as-printed SLM $Al_{0.3}CoCrFeNi$ HEA compared with as-cast or wrought counterparts, while maintaining significant ductility. Quantitative accounting of the various contributions to the yield strength demonstrates the important role played by the high in-built dislocation density.

## ACKNOWLEDGEMENTS

This work was financed by the AID (Agence de l'innovation de défense) and DGA (Direction Générale de l'Armement). Florian Peyrouzet and Stéphane Gorsse thank the LabEx AMADEus (ANR-10-LABX-42) and IdEx Bordeaux (ANR-10-IDEX-03-02) for support through the Investissements d'Avenir programme of the French Government managed by the Agence Nationale de la Recherche. The authors thank Muriel Veron (Université Grenoble Alpes, CNRS, Grenoble INP, SIMaP) for carrying out EBSD-TEM analysis on ASTAR.

## ELECTRONIC SUPPLEMENTARY MATERIAL

The online version of this article (https://doi.org/10.1007/s11837-019-03715-1) contains supplementary material, which is available to authorized users.

## REFERENCES

1. B. Cantor, I.T.H. Chang, P. Knight, and A.J.B. Vincent, *Mater. Sci. Eng. A* 375, 213 (2004).
2. J.W. Yeh, S.K. Chen, S.J. Lin, J.Y. Gan, T.S. Chin, T.T. Shun, C.H. Tsau, and S.Y. Chang, *Adv. Eng. Mater.* 6, 299 (2004).
3. D.B. Miracle and O.N. Senkov, *Acta Mater.* 122, 448 (2017).
4. S. Gorsse, D.B. Miracle, and O.N. Senkov, *Acta Mater.* 135, 177 (2017).
5. O.N. Senkov, D.B. Miracle, K.J. Chaput, and J.-P. Couzinie, *J. Mater. Res.* 33, 3092 (2018).
6. S. Gorsse, M.H. Nguyen, O.N. Senkov, and D.B. Miracle, *Data Brief* 21, 2664 (2018).
7. S. Gorsse, J.-P. Couzinié, and D.B. Miracle, *C. R. Phys.* 19, 721 (2018).
8. S. Gorsse, C. Hutchinson, M. Gouné, and R. Banerjee, *Sci. Technol. Adv. Mater.* 18, 584 (2017).
9. S. Chen, Y. Tong, and P.K. Liaw, *Entropy* 20, 937 (2018).
10. Y. Brif, M. Thomas, and I. Todd, *Scr. Mater.* 99, 93 (2015).
11. J. Joseph, T. Jarvis, X. Wu, N. Stanford, P. Hodgson, and D.M. Fabijanic, *Mater. Sci. Eng. A* 633, 184 (2015).
12. V. Ocelik, N. Janssen, S.N. Smith, and J.T.H.M. De Hosson, *JOM* 68, 1810 (2016).
13. J. Joseph, N. Stanford, P. Hodgson, and D.M. Fabijanic, *Scr. Mater.* 129, 30 (2017).
14. A. Piglione, B. Dovgyy, C. Liu, C.M. Gourlay, P.A. Hooper, and M.S. Pham, *Mater. Lett.* 224, 22 (2018).
15. R. Li, P. Niu, T. Yuan, P. Cao, C. Chen, and K. Zhou, *J. Alloys Compd.* 746, 125 (2018).
16. H. Zhang, W. Xu, Y. Xu, Z. Lu, and D. Li, *Int. J. Adv. Manuf. Technol.* 96, 461 (2018).
17. P.D. Niu, R.D. Li, T.C. Yuan, S.Y. Zhu, C. Chen, M.B. Wang, and L. Huang, *Intermetallics* 104, 24 (2019).
18. D. Karlsson, A. Marshal, F. Johansson, M. Schuisky, M. Sahberg, J.M. Schneider, and U. Jansson, *J. Alloys Compd.* 784, 195 (2019).
19. B. Gwalani, S. Gorsse, D. Choudhuri, M. Styles, Y. Zheng, R.S. Mishra, and R. Banerjee, *Acta Mater.* 153, 169 (2018).
20. B. Gwalani, S. Gorsse, D. Choudhuri, Y. Zheng, R.S. Mishra, and R. Banerjee, *Scr. Mater.* 162, 18 (2019).
21. D. Choudhuri, B. Gwalani, S. Gorsse, M. Komarasamy, S.A. Mantri, S.G. Srinivasan, R.S. Mishra, and R. Banerjee, *Acta Mater.* 165, 420 (2019).
22. T. Niendorf, D. Leuders, A. Riemer, H.A. Richard, T. Tröster, and D. Schwarze, *Metall. Mater. Trans. B* 44, 794 (2013).
23. A. Hadadzadeh, B.S. Amirkhiz, J. Lib, and M. Mohammadia, *Addit. Manuf.* 23, 121 (2018).
24. O. Andreau, I. Koutiri, P. Peyre, J.-D. Penot, N. Saintier, E. Pessard, T. De Terris, C. Dupuy, and T. Baudine, *J. Mater. Process. Technol.* 264, 21 (2019).
25. Z. Sun, X. Tan, S.B. Tor, and C.K. Chua, *NPG Asia Mater.* 10, 127 (2018).
26. S.-H. Sun, K. Hagihara, and T. Nakano, *Mater. Des.* 140, 307 (2018).
27. H.L. Wei, J. Mazumder, and T. DebRoy, *Sci. Rep.* 5, 16446 (2015).
28. X. Zhou, K. Li, D. Zhang, X. Liu, J. Ma, W. Liu, and Z. Shen, *J. Alloys Compd.* 631, 153 (2015).
29. J. Olsen, X. Zhou, Y. Zhong, L. Liu, D. Wang, C. Yu, Y. Wang, K. Li, L. Xing, J. Ma, D. Cui, W. Liu, and Z. Shen, *Mater. Sci. Eng.* 219, 012036 (2017).
30. M.S. Pham, B. Dovgyy, and P.A. Hooper, *Mater. Sci. Eng. A* 704, 102 (2017).
31. Y.J. Yin, J.Q. Sun, J. Guo, X.F. Kan, and D.C. Yang, *Mater. Sci. Eng. A* 744, 773 (2019).
32. Y. Hong, C. Zhou, Y. Zheng, L. Zhang, J. Zheng, X. Chena, and B. An, *Mater. Sci. Eng. A* 740–741, 420 (2019).
33. S.G. Ma, S.F. Zhang, J.W. Qiao, Z.H. Wang, M.C. Gao, Z.M. Jiao, H.J. Yang, and Y. Zhang, *Intermetallics* 54, 104 (2014).

34. G.K. Williamson and W.H. Hall, *Acta Metall.* 1, 22 (1953).
35. G.K. Williamson and R.E. Smallman III, *Philos. Mag.* 1, 34 (1956).
36. B. Clausen, *Characterisation of Polycrystal Deformation by Numerical Modelling and Neutron Diffraction Measurements* (Roskilde: Ris0 National Laboratory, 1997).
37. M. Klimova, N. Stepanov, D. Shaysultanov, R. Chernichenko, N. Yurchenko, V. Sanin, and S. Zherebtsov, *Materials* 11, 53 (2018).